Geophysical Research Letters

RESEARCH LETTER
10.1029/2024GL110000

Special Collection:
Science from the Surface Water and Ocean Topography Satellite Mission

Submesoscale Eddies Detected by SWOT and Moored Observations in the Northwestern Pacific

Zhiwei Zhang[1,2,3], Mingfang Miao[1,4], Bo Qiu[5], Jiwei Tian[1,2,3], Zhao Jing[1,3], Ge Chen[3,4], Zhaohui Chen[1,3], and Wei Zhao[1,2,3]

[1]Frontier Science Center for Deep Ocean Multispheres and Earth System (FDOMES) and Physical Oceanography Laboratory/Key Laboratory of Ocean Observation and Information of Hainan Province, Sanya Oceanographic Institution, Ocean University of China, Qingdao/Sanya, China, [2]Sanya Oceanographic Laboratory, Sanya, China, [3]Laoshan Laboratory, Qingdao, China, [4]Department of Marine Technology, Ocean University of China, Qingdao, China, [5]Department of Oceanography, University of Hawaii at Manoa, Honolulu, HI, USA

Abstract The Surface Water and Ocean Topography (SWOT) mission provides a good opportunity to study fine-scale processes in the global ocean but whether it can detect balanced submesoscale eddies is uncertain due to the "contamination" by unbalanced inertial gravity waves. Here, based on concurrent observations from SWOT and a mooring array in the northwestern Pacific, we successfully captured two submesoscale cyclonic eddies with negative sea level anomalies (SLAs) in spring 2023. We find that the SLA amplitude and equivalent radius of the first (second) eddy are 2.5 cm and 16.0 km (2.0 cm and 18.8 km), respectively. For both eddies, their vertical scales are around 150 m and their horizontal velocities and Rossby numbers exceed 15.0 cm/s and 0.4, respectively. Further analysis suggests that similar submesoscale eddies can commonly occur in the northwestern Pacific and that SWOT is capable to detect larger submesoscale eddies with scales greater than ~10 km.

Plain Language Summary The Surface Water and Ocean Topography (SWOT) mission measures sea surface heights with a spatial resolution an order of magnitude higher than the prior nadir altimetry missions. However, whether SWOT can detect oceanic submesoscale eddies that play key roles in oceanic energy cycle and vertical material transports, is uncertain. To investigate this issue, we deployed a mooring array beneath a SWOT orbital swath in the northwestern Pacific. Based on the concurrent SWOT and mooring data, we successfully captured two submesoscale cyclonic eddies in spring 2023. Radii of the submesoscale eddies are found to be between 10 and 20 km and their horizontal velocities exceed 15.0 cm/s. The ratio between their vertical relative vorticity and the planetary vorticity exceeds 0.4. Further analysis suggests that similar submesoscale eddies can commonly occur in the northwestern Pacific. This study demonstrates the capability of SWOT to detect submesoscale eddies in the global ocean.

Key Points:

- Two submesoscale cyclonic eddies (SCEs) were observed by SWOT and moorings in the northwestern Pacific
- Kinematic and dynamic features of the SCEs were revealed
- It is feasible to use SWOT data to detect larger submesoscale eddies in the ocean

Supporting Information:

Supporting Information may be found in the online version of this article.

Correspondence to:

W. Zhao,
weizhao@ouc.edu.cn

Citation:

Zhang, Z., Miao, M., Qiu, B., Tian, J., Jing, Z., Chen, G., et al. (2024). Submesoscale eddies detected by SWOT and moored observations in the northwestern Pacific. *Geophysical Research Letters*, *51*, e2024GL110000. https://doi.org/10.1029/2024GL110000

Received 1 MAY 2024
Accepted 14 JUL 2024

1. Introduction

Submesoscale processes (submesoscales) are a class of oceanic motions that have spatial and temporal scales of O(0.1–10) km and O(0.1–10) days in middle latitudes, respectively (McWilliams, 2016; Thomas et al., 2008; Z. Zhang, 2024). Dynamically, submesoscales have the intermediate length scales between quasi-geostrophic mesoscale eddies and ageostrophic microscale turbulence; their momentum balance is governed by the combination of geostrophy and nonlinearity and they can induce large vertical velocities (Taylor & Thompson, 2023). Due to these dynamic natures, submesoscales play key roles in both oceanic energy cascade and vertical material/tracer transports (Capet et al., 2008; D'Asaro et al., 2011; Su et al., 2018; Yu et al., 2019; Z. Zhang et al., 2021; Qiu et al., 2022). As a result, they may significantly modulate the larger-scale oceanic dynamics, biogeochemical processes, and air-sea interactions (Guo et al., 2024; Mahadevan, 2016; Sasaki et al., 2014; Siegelman et al., 2020; Z. Zhang, 2024; Z. Zhang et al., 2023; J. Zhang et al., 2023), which make it a hot research topic in oceanography.

Existing studies on submesoscales are mainly based on geophysical fluid dynamics theories, submesoscale permitting simulations, and fragmental high-resolution remote sensing and in situ observations. Global observations targeted specifically on submesoscales are still lacking. Global sea surface height (SSH) measurements from nadir-looking satellite altimeters such as TOPEX/Poseidon, Jason, and Sentinel have significantly improved our knowledge of mesoscale eddies that have horizontal scale of O(100–500) km and account for the majority of

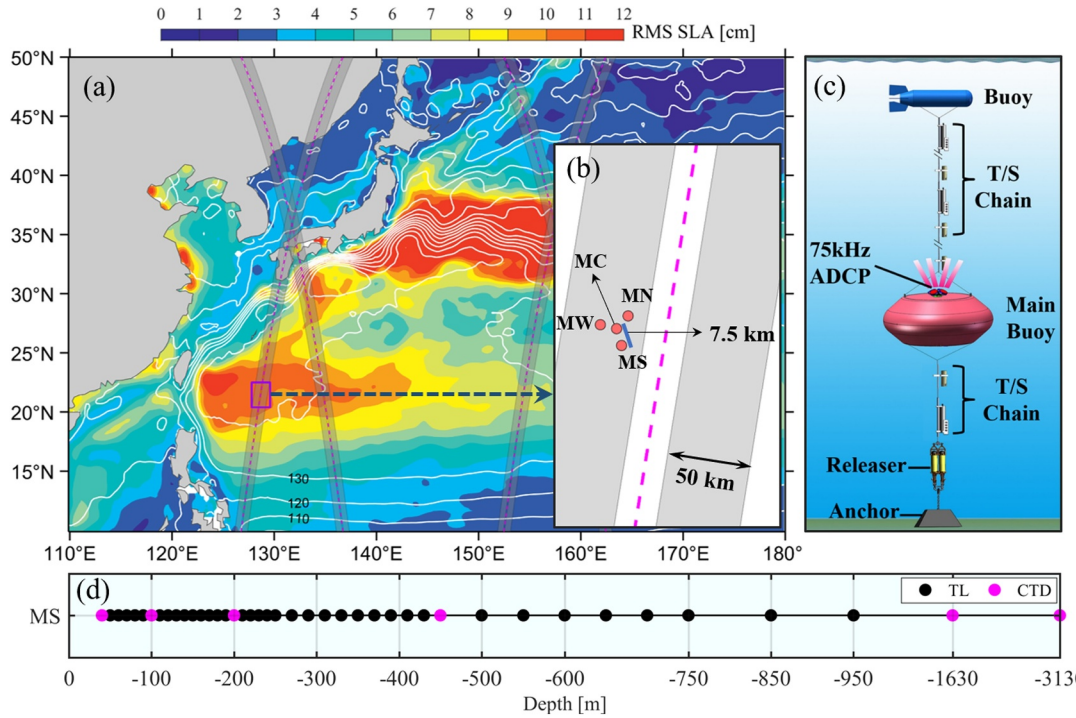

Figure 1. (a) Dynamic background and SWOT tracks in the study region. Purple dashed lines and gray shadings denote nadir track and wide swaths of SWOT during the CalVal period, respectively. Color shading denotes the root-mean-squared mesoscale sea level anomalies (SLA) and white contours are the long-term mean sea surface height, which are obtained from the DUACS data according to Miao et al. (2023). (b) Zoom in on moored observation region marked by purple rectangle in (a). Pink dots denote locations of the moorings. (c) Schematic diagram of the configuration of the mooring. Names of the instruments are marked in the diagram. (d) The designed depths of CTDs (purple dots) and temperature loggers (black dots) mounted on the mooring MS.

the oceanic kinetic energy (Abdalla et al., 2021; Ferrari & Wunsch, 2009; Fu et al., 2010; Klein et al., 2019). However, the nadir-looking altimeters can only resolve oceanic processes with horizontal scales larger than 100 km (Chelton et al., 2011; Fu et al., 2010) and thus have missed smaller mesoscale eddies and nearly all submesoscales (Klein et al., 2019). In order to improve the spatial resolution of SSH measurements and extend the measurements to submesoscales, the Surface Water and Ocean Topography (SWOT) SAR-interferometry wide-swath altimeter was designed and successfully launched in December 2022 (Fu et al., 2024). The SWOT measures the SSH along a 120-km swath that has a 20-km gap in the middle; in the center of the gap, sea level is measured by a conventional nadir altimeter (Figure 1). In a swath, the SWOT provides two-dimensional level-3 SSH maps with a 2-km spacing grid (Durand et al., 2010; Fu & Ubelmann, 2014; Morrow et al., 2019; Wang et al., 2019). The SWOT was placed in the fast calibration and validation (CalVal) orbit with a repeat cycle of ∼1 day between 29 March and 11 July 2023. After the CalVal period, it switched to the science orbit with a repeat cycle of 21 days.

With a 2-km horizontal resolution, the level-3 SSH data from SWOT has a potential to detect submesoscales in the global ocean (Fu et al., 2024). However, the SWOT-measured SSH data not only contain signals of balanced mesoscale eddies and submesoscales but also contain contributions by inertial gravity waves (IGWs). Given that IGWs have spatial scales of O(1–100) km and periods shorter than a couple of days, their SSH signals behave as "noises" when exploring submesoscales (e.g., Qiu et al., 2017, 2018; Torres et al., 2018). Though most coherent internal tides (ITs) can be removed (e.g., Dushaw et al., 2011; Ray & Zaron, 2011; Zaron, 2015, 2017, 2019), the sea level anomalies (SLAs) resulting from incoherent ITs and supertidal IGWs still have root mean square (RMS) values of several centimeters (e.g., Miao et al., 2021, 2023; Savage et al., 2017). This means that whether the SWOT data can truly capture submesoscales depends on the relative magnitudes of SSH anomalies of submesoscales and unremoved incoherent ITs and supertidal IGWs. Therefore, exploring features of submesoscales using the existing SWOT data is still a challenging task, and the identified candidate submesoscales from SWOT data need to be confirmed by other independent observations.

In this study, by combining SSH data from SWOT and traditional nadir-looking altimeters and in situ data from a mooring array, we observed two submesoscale eddies in the northwestern Pacific Subtropical Countercurrent (STCC) region where both submesoscales and IGWs are abundant (Miao et al., 2023; Qiu et al., 2014; Z. Zhang et al., 2021; Zhao, 2014). Furthermore, both surface and subsurface characteristics of these submesoscle eddies were revealed. The remainder of this paper is organized as follows. Section 2 describes the data we used. Sections 3 and 4 describe the characteristics of submesoscale eddies based on SWOT data and moored data, respectively. Summary and discussion of the paper are given in Section 5.

2. Data

2.1. Altimetry Data

During the 1-day repeat CalVal period between 29 March and 11 July 2023, Pass 021 of the SWOT crossed the subtropical northwestern Pacific (Figure 1). Here, the level-3 2 km × 2 km gridded SSH data (expert version 1.0) along this Pass were used. In addition to the SWOT data, the level-4 SSH product from Copernicus Marine Service were also used. It was constructed by the Data Unification and Altimeter Combination System (DUACS) based on along-track measurements by multi-mission nadir altimeters. Spatial and temporal resolutions of the DUACS data are 1/4° and one day, respectively (Taburet et al., 2019). Note that both the SWOT and DUACS SSH data have removed the SLA of coherent ITs using the method in Zaron (2019). In order to have a fair comparison between the two data sets, the SLAs were computed by subtracting their corresponding time means during the CalVal period.

2.2. Moored Data

As a part of the Adopt-A-Crossover consortium to support the SWOT CalVal mission, the Ocean University of China initiated the North West Pacific campaign, and deployed four moorings under the SWOT Pass 021 in the northwestern Pacific STCC region (Figures 1a and 1b). The moorings were deployed between 27 July 2022 and 26 June 2023, which had a 90-day overlap with the CalVal period. Moorings MS, MW, and MN constitute an equilateral triangle and mooring MC (at 128.49°E, 21.48°N) is located at the center of this triangle. Distances from the mooring MC to the other moorings are all 7.5 km. The four moorings were all equipped with an upward-looking 75 kHz acoustic Doppler current profiler (ADCP; Figure 1c) whose temporal sampling interval and vertical resolution were set as 30 min and 16 m, respectively. The ADCPs on moorings MS, MW, MN, and MC measured velocity profiles between 40–425, 40–465, 40–585, and 40–605 m, respectively. In addition, the three outside moorings (i.e., MS, MW, and MN) were also equipped with temperature/salinity (T/S) chains. Given that the moorings MW and MN did not have T/S measurements above 80 and 200 m, respectively, only the T/S data from mooring MS were used. T/S chain of mooring MS consisted of 36 SBE56 temperature loggers and 6 SBE37 Conductivity-Temperature-Depth (CTD) measurements. Vertical resolutions of the temperature measurements are 10, 20, 50, and 100 m between 40–250, 250–450, 450–750, and 750–950 m, respectively (Figure 1d). Sampling interval of the temperature measurements is 5 min. More detailed information of the four moorings can be found in Table S1 of Supporting Information S1.

Processing of the moored data is similar to our previous mooring-based studies (e.g., Miao et al., 2021, 2023; Z. Zhang et al., 2016, 2021). Specifically, we firstly converted raw velocities and temperatures into hourly data through time averaging. Then, the hourly data were linearly interpolated onto the uniform 5-m vertical grids. We removed IGW signals by applying the fourth-order Butterworth lowpass filter to the hourly data with a cutoff period of 48 hr (the local inertial period is 32.7 hr).

3. Submesoscale Signals Observed by SWOT

Given that the DUACS data fail to capture the submesoscales while the SWOT data can potentially resolve them, we use the SLA difference (ΔSLA) between SWOT and DUCAS data to explore the candidate submesoscale signals in our study region. Through examining the 90-day ΔSLA maps during the CalVal period, we detected two cases of submesoscale eddy-like signals near the moorings in mid April and mid May 2023, respectively. For the first case, the DUACS data clearly shows a mesoscale anticyclonic eddy with positive SLAs in the mooring region (Figure 2a). The diameter of this anticyclonic eddy is larger than 200 km and its maximum SLA exceeds 16 cm. With respect to the concurrent SWOT data, it also shows the existence of this mesoscale anticyclonic eddy but the SLA distribution is much rougher with some fine-scale signals superimposed on it (Figure 2b). These fine-scale

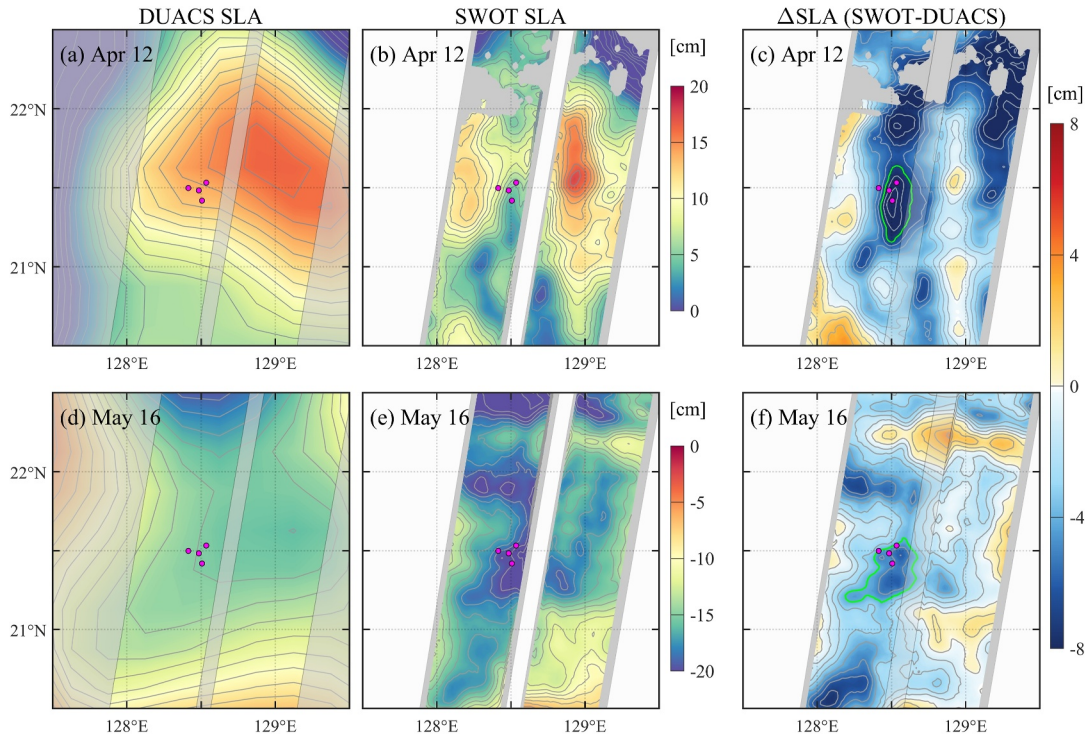

Figure 2. Maps of SLAs from (a) DUACS product and (b) SWOT level-3 data on 12 April 2023. Gray lines are the SLA contours with an interval of 1 cm. (c) The difference between (b) and (a). Gaps between two swaths of SWOT were filled through linear interpolation. Green line denotes the −7 cm contour, which is the outmost closed Δ*SLA* contour of the detected submesoscale cyclone. Purple dots denote mooring locations. (d, e, f) Same as (a, b, c) but for results on 16 May 2023. Green line in (f) denotes the Δ*SLA* contour of −4 cm.

signals can be seen more clearly in the distribution of Δ*SLA* (Figure 2c). It shows many closed positive and negative Δ*SLA* contours with scales smaller than 50 km, which look like submesoscale eddies with circular and elliptic shapes. Particularly, negative Δ*SLA* contours like a submesoscale cyclonic eddy (SCE) occurred at the mooring locations in mid April 2023. The largest negative Δ*SLA* of this SCE-like structure reaches −9.5 cm (defined at its center). If we define the outermost closed contour of Δ*SLA* surrounding the center as boundary of the SCE-like structure, its equivalent radius is estimated to be 16.0 km (i.e., radius of the circle that has the same area). The SLA amplitude of this SCE-like structure defined by the absolute Δ*SLA* difference between the center and boundary is 2.5 cm.

With respect to the second case, the DUACS SLA shows a mesoscale cyclonic eddy (negative SLA values) in mid May 2023 in the mooring region (Figure 2d). This cyclonic eddy seems to have two centers and its diameter also exceeds 200 km. Similar to the first case, the SWOT SLA also reveals rich finer-scale structures (Figure 2e). Although the SWOT SLA is also dominated by negative values, it has localized maximums whose SLA values are much lower than the DUACS result. The map of Δ*SLA* also shows many closed contours of positive and negative Δ*SLA* (Figure 2f). They are superimposed on the mesoscale cyclonic eddy and their scales are also smaller than 50 km. At the mooring locations, there is also a SCE-like structure whose largest negative Δ*SLA* is −6.0 cm. The SLA amplitude and equivalent radius of this SCE-like structure are 2.0 cm and 18.8 km, respectively.

The above comparisons between the SWOT and DUACS SLAs suggest that the SWOT observations can capture submesoscales-like signals with spatial scales smaller than 50 km that are missing in the traditional nadir-looking altimeter data. To further examine these submesoscales-like signals, we compare the time series of SWOT and DUACS SLAs in Figure 3a. Here, both the SLA time series are interpolated onto the mooring site MS where we have concurrent moored velocity and temperature data. The two time series are overall consistent with each other on the mesoscale time scale (longer than ∼16 days) and their correlation coefficient (r) during the CalVal period is 0.96. For example, they both revealed prominent positive SLAs of a mesoscale anticyclonic eddy and negative SLAs of a mesoscale cyclonic eddy as shown in Figure 2. Different from the smooth DUACS SLA, however, the

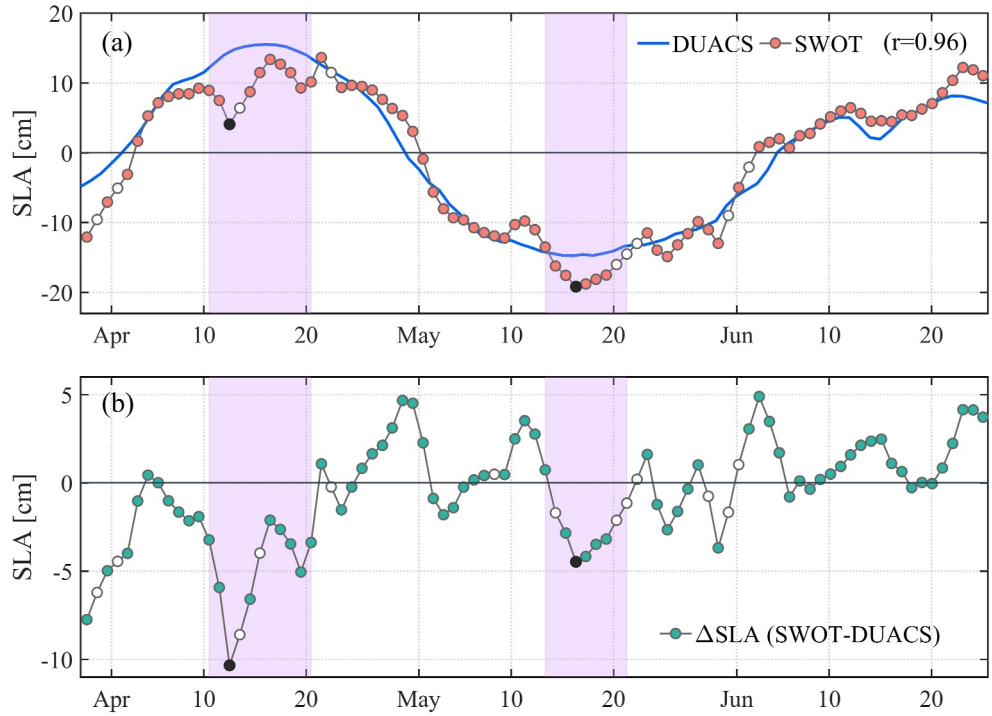

Figure 3. (a) Time series of SLAs from DUACS product (blue line) and SWOT level-3 data (gray dotted line) at the mooring MS. Correlation coefficient of the two time series is marked. White circles denote missing data filled using linear interpolation. Purple shadings mark the periods of the two submesoscale cyclonic eddy-like signals. Black circles mark the 2 days shown in Figure 2. (b) Difference between the SWOT and DUACS-derived SLA time series in (a).

SWOT SLA shows many submesoscales-like signals with amplitudes smaller than 10 cm. They are superimposed on the mesoscale eddies but have much shorter time scales. The above difference between SWOT and DUACS SLAs can also be seen from their power spectra (Figure S1 in Supporting Information S1). Specifically, the spectra of the two time series nearly overlap each other at periods longer than 16 days, but the power spectral density of SWOT SLA is significantly larger than the DUACS result at periods shorter than 16 days. Note that both the above SCE-like structures were accompanied by mesoscale eddies, which agrees with the previous finding that generation of submesoscales is closely associated with deformation of mesoscale eddies (McWilliams, 2016; J. Zhang et al., 2023).

The above two SCE-like structures in the mooring region can be also clearly seen from the time series of SWOT SLA (Figures 3a and 3b). For the first and second cases, the negative ΔSLA between SWOT and DUACS data lasts for 15 and 9 days, respectively. During the SWOT CalVal period, there are also other positive and negative ΔSLA events with periods shorter than 16 days but their amplitudes are smaller than the above two SCE-like structures. In the following, we will focus on these two SCE-like structures and demonstrate that they are indeed SCEs by combining the moored observations.

4. Characteristics of Submesoscales Revealed by Moorings

In Figure 4a, we show the mooring-observed subinertial zonal velocity (U) and temperature during the 90-day overlapped period with the SWOT CalVal phase. Similar to the SWOT SLA, mooring-observed U and isotherms also show evident oscillations with periods of $O(10)$ days which ride on the longer-period mesoscale signals. These shorter-period signals primarily occur in the upper 200 m, whose vertical scales are smaller than the mesoscale signals. Comparisons between the SWOT and mooring time series (Figure 3 vs. Figure 4a) suggest that the shorter-period signals in mid April and mid May 2023 corresponded to the abovementioned two SCE-like structures. Given that the submesoscales-like signals observed by SWOT have periods shorter than 16 days (Figure S1 in Supporting Information S1), we calculated the U anomalies associated with the two SCE-like events using a 16-day high-pass filter (fourth-order Butterworth), whose depth-time plots are shown in Figures 4b and

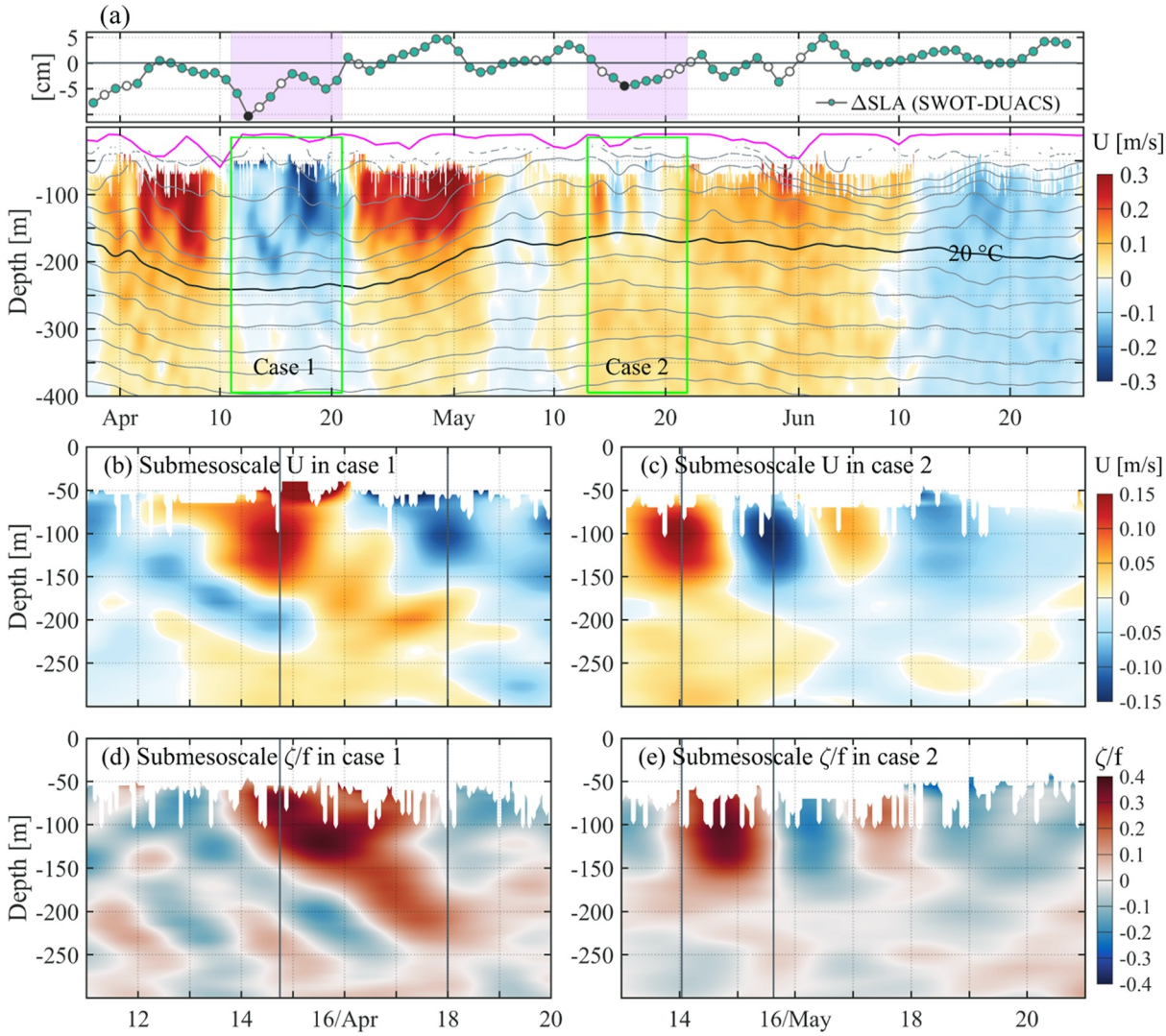

Figure 4. (a) Depth-time plots of subinertial zonal velocities from mooring MC. Gray lines denote isotherms (from mooring MS) with a contour interval of 1°C. The 20°C isotherm is marked using black line. Green rectangles mark the periods of the SCEs. Purple line denotes mixed layer depth from the Global Ocean Physics Reanalysis product. For a better comparison, the time series of in Figure 3b is also shown at the top of this figure. (b) Depth-time plot of submesoscale zonal velocities from mooring MC between 11 April and 20 April 2023 (i.e., Case 1). Submesoscale velocities are obtained by applying a 16-day high-pass filter to subinertial velocities. Gray solid lines denote the time of the maximum positive and negative velocities. (c) Same as (b) but for the Case 2 between 13 May and 21 May 2023. (d, e) Same as (b, c) but for Rossby numbers (i.e., relative vorticity divided by planetary vorticity).

4c, respectively. For both cases, the magnitude of U anomalies gradually decreased with an increasing depth until it became trivial below ~200 m; the maximum magnitude of the observed U anomalies reached ~15.0 cm/s at 50–150 m depths but it should exceed this value at surface as the SCE-like structures are surface intensified. The U anomalies of both cases changed from positive to negative with time, which corresponded to the southward migration tendency of the two SCE-like structures as seen from the sequential SWOT data (Figure S2 in Supporting Information S1). The southward migration is also supported by the results that the U anomalies at mooring MC led those at mooring MS and that the meridional velocity anomalies were much weaker than the U anomalies (Figure S3 in Supporting Information S1). Temperature anomalies of the first SCE-like structure were dominantly negative in the upper ~200 m, while they showed negative and positive alternating values for the second case (Figures S4a–S4b in Supporting Information S1). Overall, the above results demonstrate that the SWOT-detected SCE-like structures presented in Figures 2 and 3 are indeed SCEs.

To gain further insight into the dynamic features of the two SCEs, we calculated the relative vorticity using velocities from the four moorings through the Stokes' theorem $\zeta = \frac{1}{A}\oint \vec{V'} \cdot \vec{dl}$ (Buckingham et al., 2016; Z. Zhang et al., 2021). Here, $\vec{V}'$ is subinertial velocity anomaly calculated using the 16-day high-pass filter. Based on the pressure measurements by moored CTDs, we can infer that the top part of the moorings on average had a horizontal swing distance of ~300 m (method refers to Z. Zhang et al., 2021). This distance error (compared with the 7.5 km distance between two moorings) would result in a ~4% error in the calculated ζ. In Figures 4d and 4e, we show depth-time plots of the relative vorticity divided by the planetary vorticity f (i.e., ζ/f) which roughly represents the Rossby number (Ro). As expected, both the SCEs show positive Ro in the upper 200 m. For both SCEs, the observed maximum Ro reached ~0.4 which roughly occurred at the time of zero U anomaly. Given that the central mooring MC did not exactly capture the centers of the SCEs (Figure 2 and Figure S2 in Supporting Information S1) and that the moored observations were absent in the upper 50 m, we expect that the largest Ro of the SCEs (at their centers) should greatly exceed 0.4 at sea surface. For both SCEs, divergence magnitude (divided by f) of the submesoscale velocity is overall smaller than 0.2, demonstrating that the observed SCEs are quasi-balanced motions (Figures S4c and S4d in Supporting Information S1).

5. Summary and Discussion

By combining the concurrent observations from SWOT and a mooring array in the northwestern Pacific during the SWOT CalVal period, this study reported two SCEs which were missed by the traditional, coarse-resolution merged altimeter data (i.e., the DUACS product made from nadir altimeters). The SWOT data revealed that these SCEs are superimposed on mesoscale eddies in the STCC region in mid April and mid May 2023, respectively. The first SCE had an equivalent radius of 16.0 km and its SLA amplitude was 2.5 cm. With respect to the second SCE, its equivalent radius and SLA amplitude were 18.8 km and 2.0 cm, respectively. Based on the concurrent subsurface moored data, we found that the SCEs can induce short-period (<16 days) oscillations in velocity and temperature in the upper 150 m. The subsurface mooring derived horizontal velocities and Ro of the SCEs reached ~15.0 cm/s and ~0.4, respectively. Given that the SCEs were surface intensified, their true velocities and Ro at surface should be larger than these estimated values.

In addition to the above two cases of SCEs, many other submesoscale cyclone- and anticyclone-like structures with equivalent radii smaller than 25 km are also observed by the SWOT level-3 data in the subtropical northwestern Pacific (Figure S5 in Supporting Information S1). Further analysis suggests that RMS values of ΔSLA between SWOT and DUACS data during the SWOT CalVal period are overall between 2.0 and 4.5 cm (Figure S6 in Supporting Information S1). Although some of these ΔSLA signals may be caused by unbalanced incoherent ITs and supertidal IGWs (e.g., Miao et al., 2021, 2023; Qiu et al., 2018; Savage et al., 2017), our analyses shown in this study indicate that a considerable proportion of them can be caused by balanced submesoscales or fine-scale structures of mesoscale eddies which are missed in the traditional nadir altimeter data. In summary, this study demonstrates that the SWOT data has the capability to detect balanced submesoscale eddies in the subtropical northwestern Pacific.

Note that the study region has moderate activities of balanced submesoscales but relatively strong incoherent ITs (Qiu et al., 2018; Su et al., 2018; Zaron, 2017), that is, moderate signal to "noise" ratio for balanced submesoscales. This implies that it should be feasible for the SWOT data to capture balanced submesoscales in other high signal to "noise" ratio regions, such as the western boundary currents (e.g., Kuroshio Extension and Gulf Stream) and the Antarctic Circumpolar Current regions. Future analyses are called for to adopt the SWOT data to explore more kinematic features and spatiotemporal variations of submesoscales over the global oceans.

Finally, we should acknowledge that due to the absence of moored data in the upper 40 m, it is difficult to precisely quantify the respective contributions of balanced and unbalanced motions to the SWOT SSH. In Figure S7a of Supporting Information S1, we compare the SWOT SLA with the steric height at 40 m calculated using moored T/S data (Miao et al., 2021; Wang et al., 2022). Although the two time series are highly correlated ($r = 0.89$), they indeed show some differences, particularly at the submesoscale time scale (i.e., periods shorter than 16 days) and after 10 June 2023. Similar comparison also applies to the surface geostrophic velocity diagnosed from SWOT SSH and the subinertial ADCP velocity averaged between 50 and 80 m (Figure S7b in Supporting Information S1). However, based on the present data, we cannot judge whether the above differences are due to the missing moored observations in the upper 40 m or due to the remaining unbalanced SSH in the

SWOT data. Without the above knowledge, we should be cautious about the direct usage of SWOT data-derived geostrophic velocity in diagnosing energy cascade and reconstructing subsurface structures of submesoscale eddies.

Data Availability Statement

The SWOT data is provided by AVISO/DUACS (2024). The DUACS product is provided by E.U. Copernicus Marine Service Information, Marine Data Store (2023a). The GLORYS reanalysis product is provided by E.U. Copernicus Marine Service Information, Marine Data Store (2023b). The analyzed moored data is provided by Z. Zhang et al. (2024).

Acknowledgments
This study was jointly supported by the National Natural Science Foundation of China (42222601, 92258301, 42076004) and the Laoshan Laboratory Science and Technology Innovation Projects (LSKJ202201406). Data and samples were collected onboard of R/V Dongfanghong 3 implementing the cruise Northwest Pacific Comprehensive Scientific Investigation. Z. Z. is also supported by the "Taishan" Talents program (tsqn202103032) and Shandong Provincial Natural Science Foundation (ZR2023JQ013).

References

Abdalla, S., Kolahchi, A., Ablain, M., Adusumilli, S., Aich Bhowmick, S., Alou-Font, E., et al. (2021). Altimetry for the future: Building on 25 years of progress. *Advances in Space Research*, *68*(2), 319–363. https://doi.org/10.1016/j.asr.2021.01.022

AVISO/DUACS. (2024). SWOT level-3 KaRIn low rate SSH expert (v1.0) [Dataset]. *CNES*. https://doi.org/10.24400/527896/A01-2023.018

Buckingham, C. E., Naveira Garabato, A. C., Thompson, A. F., Brannigan, L., Lazar, A., Marshall, D. P., et al. (2016). Seasonality of submesoscale flows in the ocean surface boundary layer. *Geophysical Research Letters*, *43*(5), 2118–2126. https://doi.org/10.1002/2016GL068009

Capet, X., McWilliams, J. C., Molemaker, M. J., & Shchepetkin, A. F. (2008). Mesoscale to submesoscale transition in the California current system. Part III: Energy balance and flux. *Journal of Physical Oceanography*, *38*(10), 2256–2269. https://doi.org/10.1175/2008JPO3810.1

Chelton, D., Schlax, M., & Samelson, R. (2011). Global observations of nonlinear mesoscale eddies. *Progress in Oceanography*, *91*(2), 167–216. https://doi.org/10.1016/j.pocean.2011.01.002

D'Asaro, E., Lee, C., Rainville, L., Harcourt, R., & Thomas, L. (2011). Enhanced turbulence and energy dissipation at ocean fronts. *Science*, *332*(6027), 318–322. https://doi.org/10.1126/science.1201515

Durand, M., Fu, L.-L., Lettenmaier, D. P., Alsdorf, D. E., Rodríguez, E., & Esteban-Fernandez, D. (2010). The Surface Water and Ocean Topography mission: Observing terrestrial surface water and oceanic submesoscale eddies. *Proceedings of the IEEE*, *98*(5), 766–779. https://doi.org/10.1109/JPROC.2010.2043031

Dushaw, B. D., Worcester, P. F., & Dzieciuch, M. A. (2011). On the predictability of mode-1 internal tides. *Deep-Sea Research Part I*, *58*(6), 677–698. https://doi.org/10.1016/j.dsr.2011.04.002

E.U. Copernicus Marine Service Information, Marine Data Store. (2023a). Global Ocean gridded L 4 sea surface heights and derived variables nrt [Dataset]. https://doi.org/10.48670/moi-00149

E.U. Copernicus Marine Service Information, Marine Data Store. (2023b). Global Ocean physics reanalysis [Dataset]. https://doi.org/10.48670/moi-00021

Ferrari, R., & Wunsch, C. (2009). Ocean circulation kinetic energy: Reservoirs, sources, and sinks. *Annual Review of Fluid Mechanics*, *41*(1), 253–282. https://doi.org/10.1146/annurev.fluid.40.111406.102139

Fu, L.-L., Chelton, D. B., Le Traon, P.-Y., & Morrow, R. (2010). Eddy dynamics from satellite altimetry. *Oceanography*, *23*(4), 14–25. https://doi.org/10.5670/oceanog.2010.02

Fu, L.-L., Pavelsky, T., Cretaux, J.-F., Morrow, R., Farrar, J. T., Vaze, P., et al. (2024). The Surface Water and Ocean Topography mission: A breakthrough in radar remote sensing of the ocean and land surface water. *Geophysical Research Letters*, *51*(4), e2023GL107652. https://doi.org/10.1029/2023GL107652

Fu, L.-L., & Ubelmann, C. (2014). On the transition from profile altimeter to swath altimeter for observing global ocean surface topography. *Journal of Atmospheric and Oceanic Technology*, *31*(2), 560–568. https://doi.org/10.1175/JTECH-D-13-00109.1

Guo, M., Xing, X., Xiu, P., Dall'Olmo, G., Chen, W., & Chai, F. (2024). Efficient biological carbon export to the mesopelagic ocean induced by submesoscale fronts. *Nature Communications*, *15*(1), 580. https://doi.org/10.1038/s41467-024-44846-7

Klein, P., Lapeyre, G., Siegelman, L., Qiu, B., Fu, L.-L., Torres, H., et al. (2019). Ocean-scale interactions from space. *Earth and Space Science*, *6*(5), 795–817. https://doi.org/10.1029/2018ea000492

Mahadevan, A. (2016). The impact of submesoscale physics on primary productivity of plankton. *Annual Review of Science*, *8*(1), 161–184. https://doi.org/10.1146/annurev-marine-010814-015912

McWilliams, J. C. (2016). Submesoscale currents in the ocean. *Proceedings of the Royal Society*, *A472*(2189), 20160117. https://doi.org/10.1098/rspa.2016.0117

Miao, M., Zhang, Z., Qiu, B., Liu, Z., Zhang, X., Zhou, C., et al. (2021). On contributions of multiscale dynamic processes to the steric height in the northeastern South China Sea as revealed by moored observations. *Geophysical Research Letters*, *48*(14), e2021GL093829. https://doi.org/10.1029/2021GL093829

Miao, M., Zhang, Z., Zhang, J., Wang, Y., Zhao, W., & Tian, J. (2023). Steric heights of submesoscale processes and internal gravity waves in the subtropical northwestern Pacific and northern South China Sea as revealed by moored observations. *Progress in Oceanography*, *219*, 103158. https://doi.org/10.1016/j.pocean.2023.103158

Morrow, R., Fu, L.-L., Ardhuin, F., Benkiran, M., Chapron, B., Cosme, E., et al. (2019). Global observations of fine-scale Ocean surface topography with the Surface Water and Ocean Topography (SWOT) mission. *Frontiers in Marine Science*, *6*, 1–19. https://doi.org/10.3389/fmars.2019.00232

Qiu, B., Chen, S., Klein, P., Sasaki, H., & Sasai, Y. (2014). Seasonal mesoscale and submesoscale eddy variability along the North pacific subtropical countercurrent. *Journal of Physical Oceanography*, *44*(12), 3079–3098. https://doi.org/10.1175/JPO-D-14-0071.1

Qiu, B., Chen, S., Klein, P., Wang, J., Torres, H., Fu, L.-L., & Menemenlis, D. (2018). Seasonality in transition scale from balanced to unbalanced motions in the world ocean. *Journal of Physical Oceanography*, *48*(3), 591–605. https://doi.org/10.1175/JPO-D-17-0169.1

Qiu, B., Nakano, T., Chen, S., & Klein, P. (2017). Submesoscale transition from geostrophic flows to internal waves in the northwestern Pacific upper ocean. *Nature Communications*, *8*(1), 14055. https://doi.org/10.1038/ncomms14055

Qiu, B., Nakano, T., Chen, S., & Klein, P. (2022). Bi-Directional energy cascades in the pacific ocean from equator to subarctic gyre. *Geophysical Research Letters*, *49*(8), e2022GL097713. https://doi.org/10.1029/2022GL097713

Ray, R. D., & Zaron, E. D. (2011). Non-stationary ITs observed with satellite altimetry. *Geophysical Research Letters*, *38*(17), L17609. https://doi.org/10.1029/2011GL048617

Sasaki, H., Klein, P., Qiu, B., & Sasai, Y. (2014). Impact of oceanic-scale interactions on the seasonal modulation of ocean dynamics by the atmosphere. *Nature Communications*, *5*(1), 5636. https://doi.org/10.1038/ncomms6636

Savage, A. C., Arbic, B. K., Richman, J. G., Shriver, J. F., Alford, M. H., Buijsman, M. C., et al. (2017). Frequency content of sea surface height variability from internal gravity waves to mesoscale eddies. *Journal of Geophysical Research: Oceans*, *122*(3), 2519–2538. https://doi.org/10.1002/2016JC012331

Siegelman, L., Klein, P., Rivière, P., Torres, H. S., Thompson, A. F., Flexas, M., & Menemenlis, D. (2020). Enhanced upward heat transport at deep submesoscale ocean fronts. *Nature Geoscience*, *13*(1), 50–55. https://doi.org/10.1038/s41561-019-0489-1

Su, Z., Wang, J., Klein, P., Thompson, A. F., & Menemenlis, D. (2018). Ocean submesoscales as a key component of the global heat budget. *Nature Communications*, *9*(1), 775. https://doi.org/10.1038/s41467-018-02983-w

Taburet, G., Sanchez-Roman, A., Ballarotta, M., Pujol, M. I., Legeais, J. F., Fournier, F., et al. (2019). Duacs DT2018: 25 years of reprocessed sea level altimetry products. *Ocean Science*, *15*(5), 1207–1224. https://doi.org/10.5194/os-15-1207-2019

Taylor, J. R., & Thompson, A. F. (2023). Submesoscale dynamics in the upper ocean. *Annual Review of Fluid Mechanics*, *55*(1), 103–127. https://doi.org/10.1146/annurev-fluid-031422-095147

Thomas, L. N., Tandon, A., & Mahadevan, A. (2008). Submesoscale processes and dynamics. In M. Hecht & H. Hasumi (Eds.), *Ocean modeling in an eddying regime, geophysical. monograph. Series* (Vol. 177, pp. 17–38). American Geophysical Union. https://doi.org/10.1029/177gm04

Torres, H. S., Klein, P., Menemenlis, D., Qiu, B., Su, Z., Wang, J., et al. (2018). Partitioning ocean motions into balanced motions and internal gravity waves: A modeling study in anticipation of future space missions. *Journal of Geophysical Research: Oceans*, *123*(11), 8084–8105. https://doi.org/10.1029/2018JC014438

Wang, J., Fu, L.-L., Haines, B., Lankhorst, M., Lucas, A. J., Farrar, J. T., et al. (2022). On the development of SWOT in situ calibration/validation for short-wavelength Ocean topography. *Journal of Atmospheric and Oceanic Technology*, *39*(5), 595–617. https://doi.org/10.1175/JTECH-D-21-0039.1

Wang, J., Fu, L.-L., Torres, H. S., Chen, S., Qiu, B., & Menemenlis, D. (2019). On the spatial scales to be resolved by the Surface Water and Ocean Topography Ka-Band Radar interferometer. *Journal of Atmospheric and Oceanic Technology*, *36*(1), 87–99. https://doi.org/10.1175/JTECH-D-18-0119.1

Yu, X., Garabato, A. C. N., Martin, A. P., Buckingham, C. E., Brannigan, L., & Su, Z. (2019). An annual cycle of submesoscale vertical flow and restratification in the upper ocean. *Journal of Physical Oceanography*, *49*(6), 1439–1461. https://doi.org/10.1175/JPO-D-18-0253.1

Zaron, E. D. (2015). Non-stationary ITs inferred from dual-satellite altimetry. *Journal of Physical Oceanography*, *45*(9), 2239–2246. https://doi.org/10.1175/JPO-D-15-0020.1

Zaron, E. D. (2017). Mapping the nonstationary IT with satellite altimetry. *Journal of Geophysical Research: Oceans*, *122*(1), 539–554. https://doi.org/10.1002/2016JC012487

Zaron, E. D. (2019). Baroclinic tidal sea level from exact-repeat mission altimetry. *Journal of Physical Oceanography*, *49*(1), 193–210. https://doi.org/10.1175/JPO-D-18-0127.1

Zhang, J., Zhang, Z., & Qiu, B. (2023). Parameterizing submesoscale vertical buoyancy flux by simultaneously considering baroclinic instability and strain-induced frontogenesis. *Geophysical Research Letters*, *50*(8), e2022GL102292. https://doi.org/10.1029/2022GL102292

Zhang, Z. (2024). Submesoscale dynamic processes in the South China Sea. *Ocean-Land-Atmosphere Research*, *3*, 0045. https://doi.org/10.34133/olar.0045

Zhang, Z., Liu, Y., Qiu, B., Luo, Y., Cai, W., Yuan, Q., et al. (2023). Submesoscale inverse energy cascade enhances Southern Ocean eddy heat transport. *Nature Communications*, *14*(1), 1335. https://doi.org/10.1038/s41467-023-36991-2

Zhang, Z., Miao, M., Qiu, B., Tian, J., Jing, Z., Chen, G., et al. (2024). Submesoscale eddies detected by SWOT and moored observations in the northwestern Pacific [Dataset]. *Harvard Dataverse*, *V1*. https://doi.org/10.7910/DVN/JJ6FOL

Zhang, Z., Tian, J., Qiu, B., Zhao, W., Chang, P., Wu, D., & Wan, X. (2016). Observed 3D structure, generation, and dissipation of oceanic mesoscale eddies in the South China Sea. *Scientific Reports*, *6*(1), 24349. https://doi.org/10.1038/srep24349

Zhang, Z., Zhang, X., Qiu, B., Zhao, W., Zhou, C., Huang, X., & Tian, J. (2021). Submesoscale currents in the subtropical upper ocean observed by long-term high-resolution mooring arrays. *Journal of Physical Oceanography*, *51*(1), 187–206. https://doi.org/10.1175/JPO-D-20-0100.1

Zhao, Z. (2014). Internal tide radiation from the Luzon Strait. *Journal of Geophysical Research: Oceans*, *119*(8), 5434–5448. https://doi.org/10.1002/2014JC010014